We are IntechOpen,
the world's leading publisher of Open Access books
Built by scientists, for scientists

4,400
Open access books available

117,000
International authors and editors

130M
Downloads

154
Countries delivered to

Our authors are among the

TOP 1%
most cited scientists

12.2%
Contributors from top 500 universities

CLARIVATE ANALYTICS
BOOK CITATION INDEX
INDEXED

WEB OF SCIENCE™

Selection of our books indexed in the Book Citation Index
in Web of Science™ Core Collection (BKCI)

Interested in publishing with us?
Contact book.department@intechopen.com

Numbers displayed above are based on latest data collected.
For more information visit www.intechopen.com

Some Basic and Key Issues of Switched-Reluctance Machine Systems

Chang-Ming Liaw, Min-Ze Lu, Ping-Hong Jhou and Kuan-Yu Chou

Abstract

Although switched-reluctance machine (SRM) possesses many structural advantages and application potential, it is rather difficult to successfully control with high performance being comparable to other machines. Many critical affairs must be properly treated to obtain the improved operating characteristics. This chapter presents the basic and key technologies of switched-reluctance machine in motor and generator operations. The contents in this chapter include: (1) structures and governing equations of SRM; (2) some commonly used SRM converters; (3) estimation of key parameters and performance evaluation of SRM drive; (4) commutation scheme, current control scheme, and speed control scheme of SRM drive; (5) some commonly used front-end converters and their operation controls for SRM drive; (6) reversible and regenerative braking operation controls for SRM drive; (7) some tuning issues for SRM drive; (8) operation control and some tuning issues of switched-reluctance generators; and (9) experimental application exploration for SRM systems: (a) wind generator and microgrid; (b) EV SRM drive.

Keywords: switched-reluctance machine, motor drive, generator system, modeling, current control, speed control, commutation shift, voltage boosting

1. Introduction

Although switched-reluctance machine (SRM) [1, 2] is not the mainstream among the existing machines, it still possesses high potentials both in motor and generator applications [3–6]. Basically, it has the following key features: (i) doubly salient and singly excited with concentrated windings and (ii) without permanent magnets and conductors on its rotor. Hence, it has a rigid structure and is suited for high-speed driving applications. In driving control, it possesses highly developed torque and acceleration capabilities. The employed converter is simple topology and has fault tolerance. However, the doubly salient structure of SRM makes it have many inherent drawbacks, such as higher torque ripple, vibration, and acoustic noise. In addition, the nonlinear winding inductance and non-ideal winding current waveform render its dynamic modeling and high-performance control more difficult to achieve. Thus, many key affairs must be treated. The typical ones include

(i) motor design [7]; (ii) power circuit design and switching control; (iii) proper rotor position sensing and commutation setting; (iv) dynamic modeling; (v) current control [8, 9]; (vi) speed control [10]; (vii) commutation shift [11–13]; (viii) voltage boosting [14–17]; (ix) field weakening via commutation shifting [11–13]; and (x) torque ripple and vibration reductions. Under high speed and/or heavy load, commutation shift with equivalent field-weakening effects is the effective way to improve the SRM winding current waveforms and thus the torque-generating capability. As the speed is further increased, the voltage boosting approach must be applied for enhancing the current tracking response. Some possible solutions will be discussed in this chapter.

SRM can be operated as a generator by properly allocating winding current at negative winding inductance slope region [18–20]. Owing to the rigid mechanical structure and ease of starting for cogging torque-free nature, SRM is suited to be a wind generator. However, the generation behaviors of SRG are also highly influenced by many critical features, especially the effects of back electromotive force (EMF), which is negative in generator mode to assist the current during demagnetizing period. The key issues affecting the performance improvement of SRG include: (i) equipment of excitation source; (ii) commutation setting and shifting [19]; (iii) current switching control. To effectively counteract the negative effects of back-EMF, the hysteresis current control PWM with hard free-wheeling is normally adopted; (iv) voltage controls [19]; and (v) power maximization control [18], etc.

From the exploration one can be aware that commutation instant tuning is the most effective way in improving the developed power and ripple characteristics of a SRG.

A suited converter for switched-reluctance machine generating quasi-square winding current waveform is needed. The surveys for SRM converters can be found in [21–24]. The asymmetric bridge converter with 2N (N = phase number) switches possesses the most flexible winding current PWM switching control capability. Therefore, it is normally adopted, especially the SRM drive with regenerative braking capability and the SRG.

2. Basics of switched-reluctance machines

2.1 Machine structures

The major features of an SRM are shown in **Figure 1**. Similar to variable-reluctance stepping motor, SRM possesses doubly salient and singly excited structure. It has toothed stator and rotor. The rotor is not equipped with neither windings nor permanent magnets. Due to its rugged structure, highly developed torque and acceleration capabilities, low cost, etc., it possesses high application potential, especially driving at high speed in harsh environments.

For speed drive applications, the stroke angle of an SRM is generally larger than a stepping motor. Generally, the four-phase 8/6, three-phase 6/4, and three-phase 12/8 SRMs are the most popularly adopted. The stroke angle θ_s and stroke rate R_s of SRM can be derived to be:

$$\theta_s = \left| \frac{360°}{n_s} - \frac{360°}{n_r} \right| = |P_s - P_r|, R_s = \frac{360°}{\theta_s} \text{ (strokes/rev)} \qquad (1)$$

where n_s = stator tooth number, n_r = rotor tooth number, P_s = stator tooth pitch, and P_r = rotor tooth pitch.
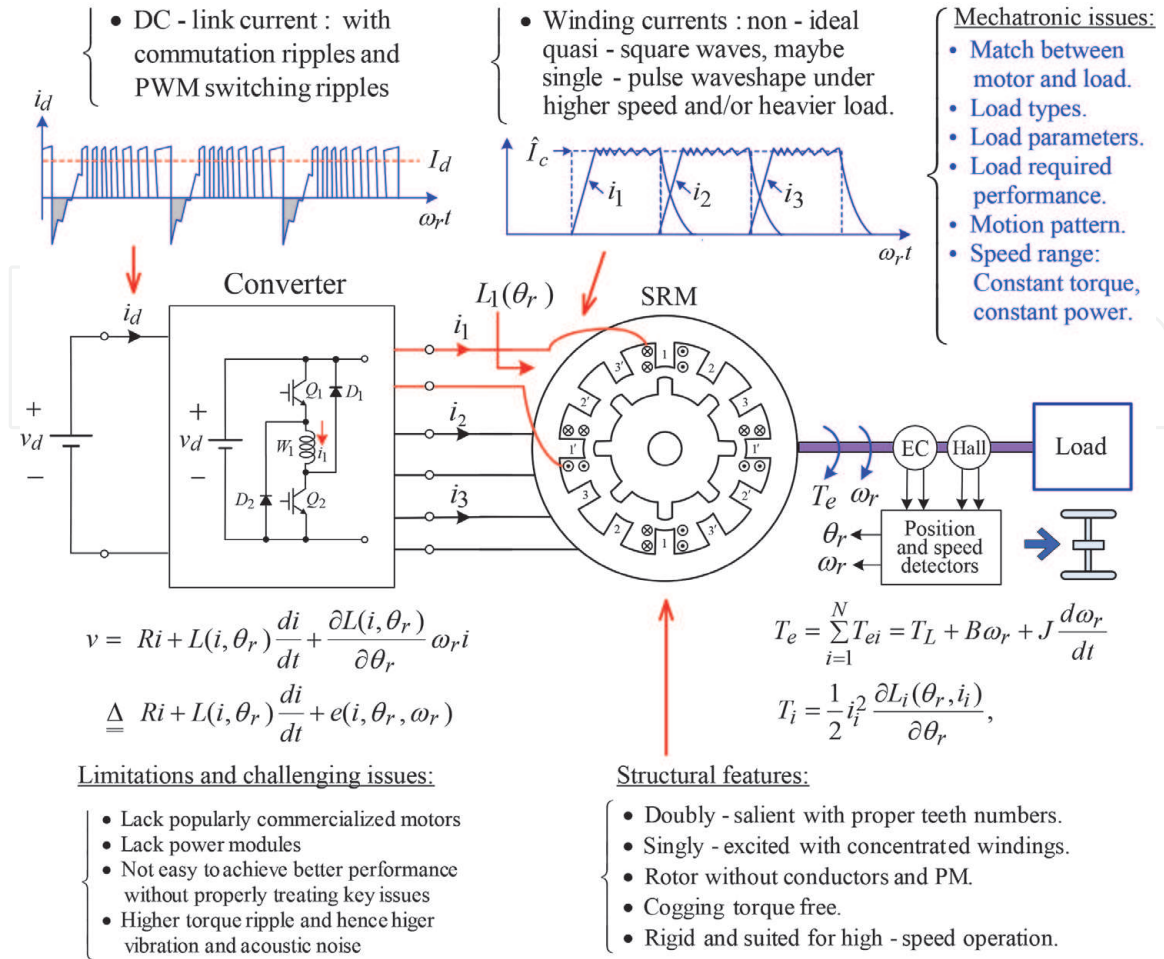
Figure 1.
Key features of switched-reluctance machines.

The stroke frequency f_{st} of an SRM with θ_s at the speed n (rpm) can be derived as:

$$f_{st} = \frac{nR}{60} = \frac{6n}{\theta_s} \tag{2}$$

2.2 Governing equations

Figure 2 shows the configuration and phase equivalent circuit of a four-phase 8/6 SRM. A simplified model of the SRM is obtained on the basis of the following assumptions: (a) no mutual flux linkage between phase windings and (b) the magnetic circuit being linear.

2.2.1 Voltage equation

The per-phase voltage equation of an SRM can be expressed as:

$$v = iR + \frac{d\lambda(i,\theta_r)}{dt} = iR + \frac{dL(i,\theta_r)}{dt} = iR + L(i,\theta_r)\frac{di}{dt} + i\omega_r\frac{\partial L(i,\theta_r)}{\partial \theta_r}$$
$$= iR + L(i,\theta_r)\frac{di}{dt} + e(i,\omega_r,\theta_r) \tag{3}$$

where v = winding terminal voltage, i = winding current, R = winding resistance, $L(i,\theta_r) \equiv L(i,\theta_r) \triangleq \partial\lambda(i,\theta_r)/\partial i$ = incremental winding inductance, $\theta_r =$
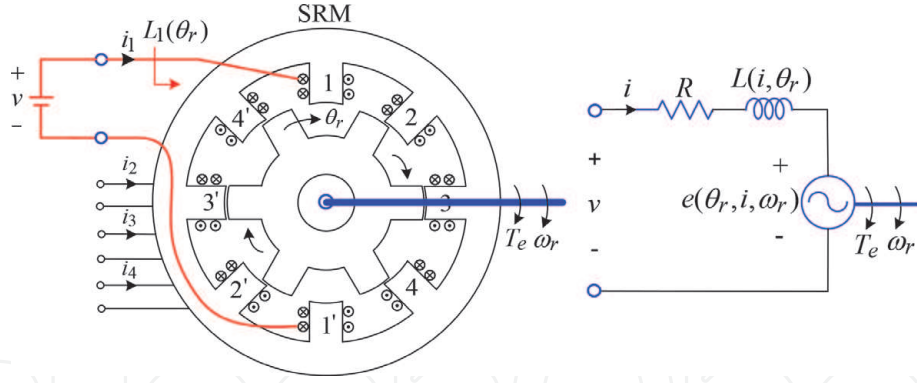
3

Figure 2.
Configuration of a four-phase SRM and its phase equivalent circuit.

rotor angle, ω_r = rotor speed, and $e(i, \omega_r, \theta_r) \triangleq [\partial L(i, \theta_r)/\partial\theta_r]i\omega_r$ = back electromagnetic force (EMF).

2.2.2 Torque equation

The developed torque T_{ei} of an SRM can be derived using energy or coenergy as:

$$T_{ei} = \left.\frac{\partial W_c(i, \theta_r)}{\partial\theta_r}\right|_{i=\text{constant}} = \frac{1}{2}i_i^2\frac{\partial L(i, \theta_r)}{\partial\theta_r} \triangleq k_t i_i^2 \qquad (4)$$

where $k_t \triangleq 0.5\partial L(i, \theta_r)/\partial\theta_r$. Accordingly, the composite electromagnetic developed torque and the mechanical equation of a N-phase SRM drive can be written as:

$$T_e = \sum_{i=1}^{N} T_{ei} = \frac{1}{2}\sum_{i=1}^{N} i_i^2\frac{\partial L(i, \theta_r)}{\partial\theta_r} = T_L + B\omega_r + J\frac{d\omega_r}{dt} \qquad (5)$$

where T_e = total electromagnetic torque, N = phase number, T_L = load torque, J = total moment of inertia, and B = total damping ratio.
Switched-reluctance generator:
In contrast to SRM drive, SRG converts mechanical input power P_i into electrical output power P_g as:

$$T_e = T_i - B\omega_r - J\frac{d\omega_r}{dt}, \quad P_e = T_e\omega_r, \quad P_g = P_e - P_c - P_{cu} \qquad (6)$$

where T_i = input shaft torque, P_e = electromagnetic developed power, P_{cu} = SRM copper loss, and P_c = SRM core loss.
Comments: From the above governing voltage and torque equations, one can be aware of the following facts:
(i) The SRM back-EMF is dependent on winding inductance slope, current, and rotor speed. (ii) The current response and the developed torque performance are affected by the back-EMF, especially under higher speed and/or heavier load. (iii) Tuning the commutation shift angle properly can improve the winding current tracking performance. As the speed is further increased, the DC-link voltage boosting approach must be applied instead. (iv) T_{ei} is proportional to the square of current. Therefore, it possesses highly developed torque like a series DC motor. (v) For operating as SRG, the generating characteristics are more sensitive to winding current waveform and commutation instant setting for the negative back-EMF. (vi) The observed torque can be obtained from Eq. (5) for achieving direct torque control.

2.3 Motor and generator operation modes

The phase winding inductance profile versus rotor position and current waveforms under motor mode and generator mode are sketched in **Figure 3**. According to Eq. (4), arranging the excitation under the region with positive or negative slope of winding inductance, an SRM can be operated as a motor or a generator.

2.4 Dynamic models

The dynamic modeling and dynamic control affairs can be referred to [2, 10, 25]. The standard SRM drive control belongs to cascade structure consisting of inner current-loop and outer speed-loop. **Figure 4(a)** shows the hypothesized control block of an SRM drive under PWM control, wherein the related variables are defined as phase current command $i_i^* \triangleq I_c S_i$, $I_c \triangleq$ current command magnitude and $S_i \equiv i$th phase switching function; $i_i \triangleq H_i(\bullet) i_i^*$ is assumed with $H_i(\bullet)$ being the ith phase closed-loop current tracking transfer function.

Figure 4(b) shows the detailed phase winding control block, wherein K_i denotes the current sensing factor. Obviously, the winding current tracking control is significantly affected by the back-EMF and nonlinear winding inductance. **Figure 4 (c)** illustrates the speed-loop control block, wherein $\bar{k}_t$ denotes the average torque-generating constant. By assuming ideal current control with $i_i \approx I_c$, the dynamic torque-generating constant is found from Eq. (5) by linearization process at an operation point $(i_i \approx I_{c0})$ as:

$$T_{e0} = \frac{1}{2} \frac{\partial L(I_{c0}, \theta_r)}{\partial \theta_r} I_{c0}^2 \qquad (7)$$
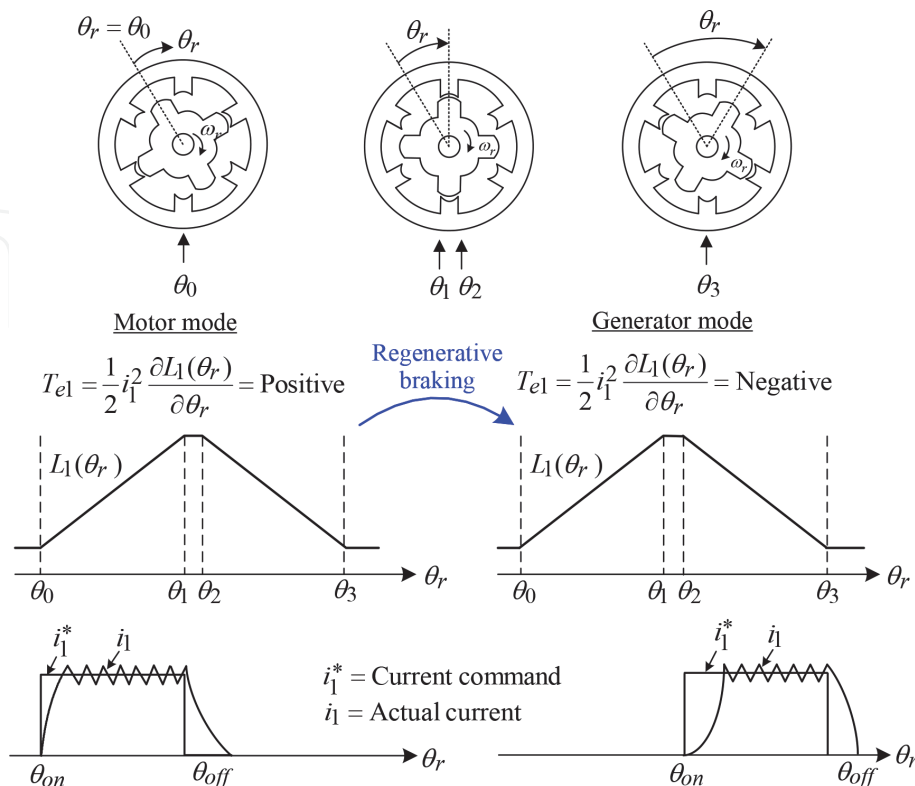

Figure 3.
Idealized phase winding inductance $L_1(\theta_r)$ and currents of an SRM in motor mode and generator mode.

$$T_e = \frac{1}{2}\frac{\partial L(I_c, \theta_r)}{\partial \theta_r}I_c^2 = \frac{1}{2}\frac{\partial L((I_{c0} + \Delta I_c), \theta_r)}{\partial \theta_r}(I_{c0} + \Delta I_c)^2 \qquad (8)$$

$$\Delta T_e = T_e - T_{e0} \approx \frac{\partial L(I_{c0}, \theta_r)}{\partial \theta_r}I_{c0}\Delta I_c \triangleq \overline{k}_t \Delta I_c \qquad (9)$$

with the dynamic torque-generating constant being:

$$\overline{k}_t \triangleq \frac{\partial L(I_{c0}, \theta_r)}{\partial \theta_r}I_{c0} \qquad (10)$$

Obviously, the torque-generating constant is not a constant; rather it is varied with the changing operating conditions. The robust controls are needed to yield better performance.

And the dynamic model depicted in **Figure 4(c)** can be represented from Eq. (5) as:

$$H_p(s) = \frac{K_\omega}{Js + B} \triangleq \frac{b}{s + a} \quad , \quad a \triangleq \frac{B}{J} \quad , \quad b \triangleq \frac{K_\omega}{J} \qquad (11)$$

where K_ω denotes the speed sensing factor.

2.5 SRM converters

There already are many existing converters for SRM drive [22–24]. Among these ones, the asymmetric bridge converter shown in **Figure 5(a)** has the most flexible PWM switching capability, and it is also the most generally adopted one for SRM drive and SRG. Two diodes and two switches are required in one phase. For each phase, the lower switch conducts commutation switching, while the upper switch is in charge of PWM switching.

Figure 5(b) sketches the typical winding current waveforms of SRM and SRG. **Figure 5(c)–(e)**, respectively, shows the schematics and current paths of three operation modes: (i) Mode-1, excitation mode; (ii) Mode-2, soft freewheeling mode; and (iii) Mode-3, demagnetization mode or hard freewheeling mode. For a current-controlled PWM (CCPWM) scheme, hard freewheeling operation will
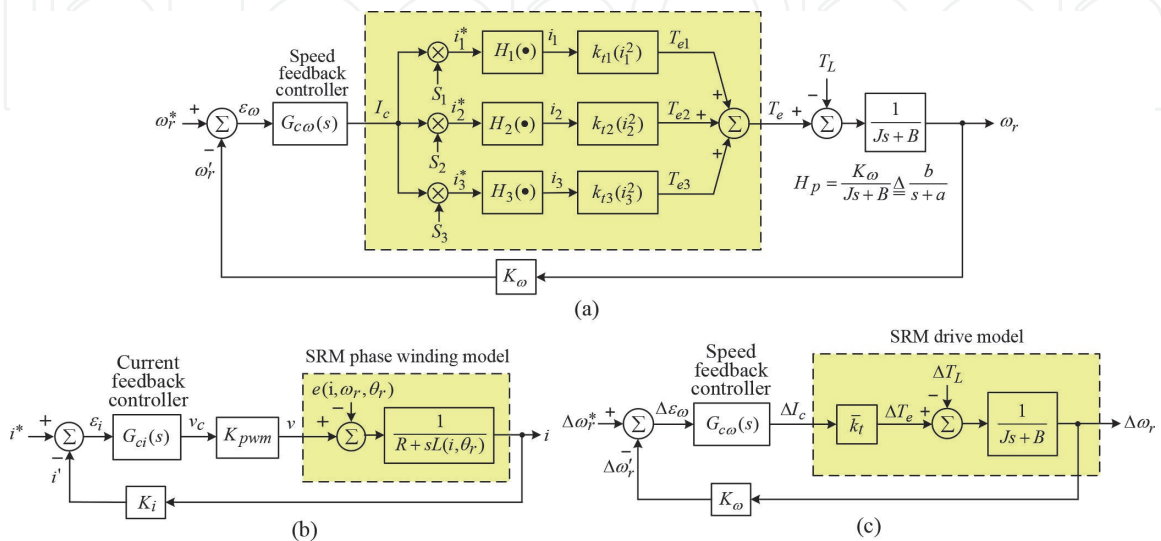

Figure 4.
Control blocks of an SRM drive with current-controlled PWM scheme: (a) hypothesized control block diagram; (b) per-phase inner current control loop; (c) outer speed control loop.
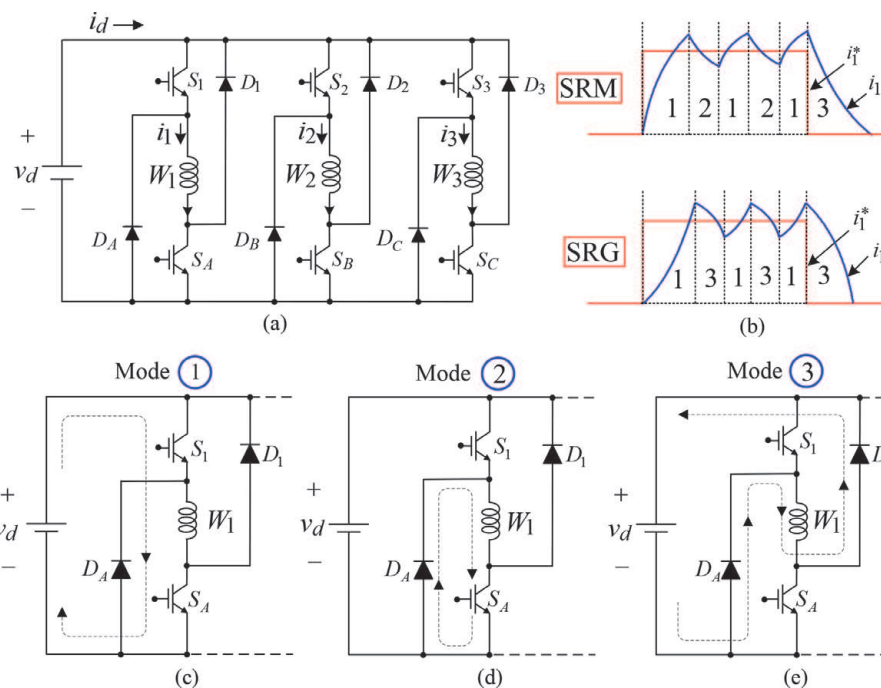
Figure 5.
Asymmetric bridge converter: (a) schematic; (b) SRM and SRG typical winding current waveforms; (c) excitation mode; (d) soft freewheeling mode; (e) demagnetization mode (or hard freewheeling mode).

cause the faster demagnetization owing to the negative demagnetizing voltage rather than zero voltage being applied. For a SRG, the hysteresis CCPWM scheme with hard freewheeling (Mode-3) is normally applied to counteract the effects of back-EMF on the winding current response.

2.6 Equivalent circuit parameter estimation and performance test of SRM drive

Figure 6 shows the suggested test facilities for establishing an SRM drive: (a) stationery test equipment for measuring the key motor parameters and variables; (b) the SRM drive running characteristics test environment using eddy current brake; and (c) the alternative SRM drive running characteristics test using load SPMSG as dynamic load. Since the accurate eddy current brake and torque meter are not available, this alternative of loading test is worth of adopting. However, the surface-mounted permanent-magnet synchronous generator (SPMSG) must be properly set, and it should be noted that the motor efficiency is both speed and load dependent.

2.6.1 DC test

Powering the stator winding with different values of the DC voltage leads to various corresponding values of the current. By calculating the sets of readings and averaging their results, a value of stator winding resistance is reasonably obtained.

2.6.2 Blocked rotor test

2.6.2.1 AC test

With the rotor being blocked at a specific position, the back-EMF is zero from Eq. (3). Hence the equivalent circuit of SRM phase winding under blocked rotor can be expressed in **Figure 6(a)**. The phase winding is excited with a variable-voltage variable-frequency AC source. At each frequency with fixed current level, the input
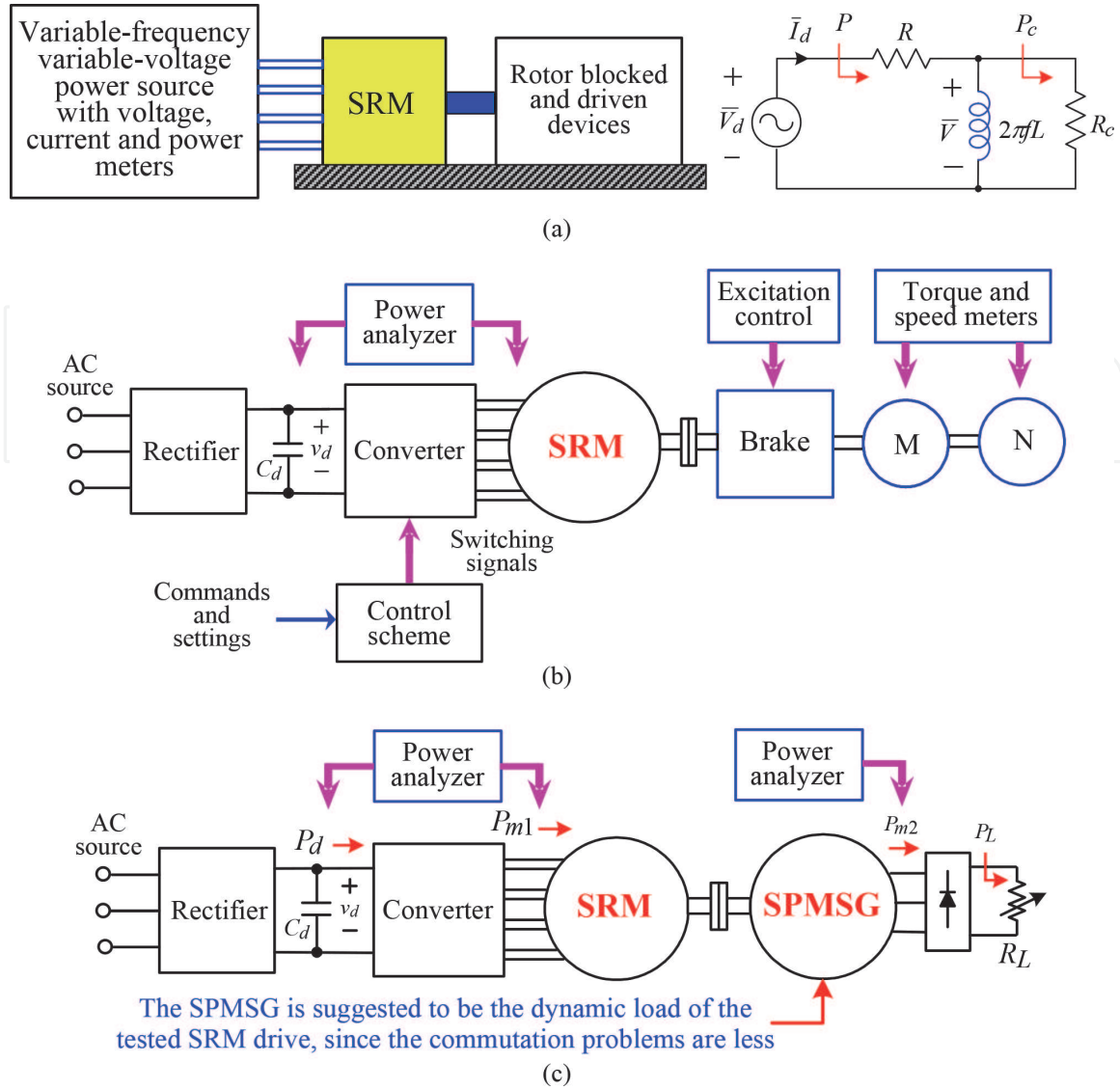
Figure 6.
Test facilities for SRM drive: (a) stationery test equipment and the equivalent circuit of SRM phase winding under blocked rotor; (b) SRM drive running characteristics test using eddy current brake; (c) SRM drive running characteristics test using load SPMSG as dynamic load.

power P, frequency f, and RMS values of the input voltage V_d and current I_d are recorded. Similarly, readings are taken at different constant currents. The same procedure is repeated with an increment of rotor position for the next rotor position till one rotor pole pitch is covered, namely, from the aligned to unaligned position of the rotor with respect to the excited stator. From the above sets of readings, the phase winding inductance at a specified excitation current, frequency, and rotor position is obtained following the well-known AC estimation approach.

With the measured P, f, V_d, and I_d, the phase winding inductance can be obtained from **Figure 6(a)** as:

$$L = \left[2\pi f \sqrt{(I_d/V)^2 - (1/R_c)^2}\right]^{-1} \tag{12}$$

where

$$\overline{V} = \overline{V}_d - \overline{I}_d R \tag{13}$$

$$P_c = P - I_d^2 R, \quad R_c = V^2/P_c \tag{14}$$

with $\overline{V}_d \equiv V_d\angle0°$, $\overline{I}_d \equiv I_d\angle\varphi$, $\overline{V} \equiv V\angle\delta$, P_c, and R_c being the core loss and its equivalent resistance.

2.6.2.2 LCR meter test

For simplicity, the above measurement procedure is conducted using LCR meter at various rotor positions under different frequencies. However, the current-dependent characteristics of winding inductance cannot be obtained, since the LCR meter is small-signal excitation.*Measured example*: The measured three-phase winding inductance profiles of a three-phase SRM (12/8, 380 V, 2000 rpm, 2.2 kW) using the LCR meter (HIOKI 3532-50 LCR HiTESTER) at 42 Hz and 267 Hz corresponding the speed of 315 rpm and 2000 rpm are shown in **Figure 7**. From **Figure 7**, one can observe that the three winding inductances are slightly unsymmetrical and have a frequency-dependent characteristic. The winding DC resistance is measured using DC excitation method as $R = 1.43\Omega$.

2.6.3 No-load test

2.6.3.1 AC test

The SRM is run forcibly at a constant speed. By exciting the SRM phase winding with AC voltage (or current), one can measure the Hall signal and rotor position modulated voltage (or current) to observe the adequacy of Hall sensor installation.

2.6.3.2 Constant current injection test

From Eq. (3) one can find that the back-EMF of a SRM is proportional to the winding exciting current and rotor speed. The constant current injection method is proposed to measure its back-EMF. The constant current source is produced by voltage-to-current converter using the power operational amplifier OPA 548 shown in **Figure 8**. The load PMSG coupled to the test SRM (four-phase, 8/6, 48 V/2.3 kW, 6000 rpm, DENSEI Company, Japan) is powered by the commercial inverter and turned at a constant speed. The measured winding terminal voltage v and quadrature Hall signals by the constant current injection at $i = 0.979A$ and $\omega_r = 3000$ rpm are also plotted in **Figure 8**. The measured voltage v is approximately equal to the back-EMF for the negligibly small winding resistance drop. From the measured results, one can be aware of the correctness of Hall sensor installation of this example SRM.
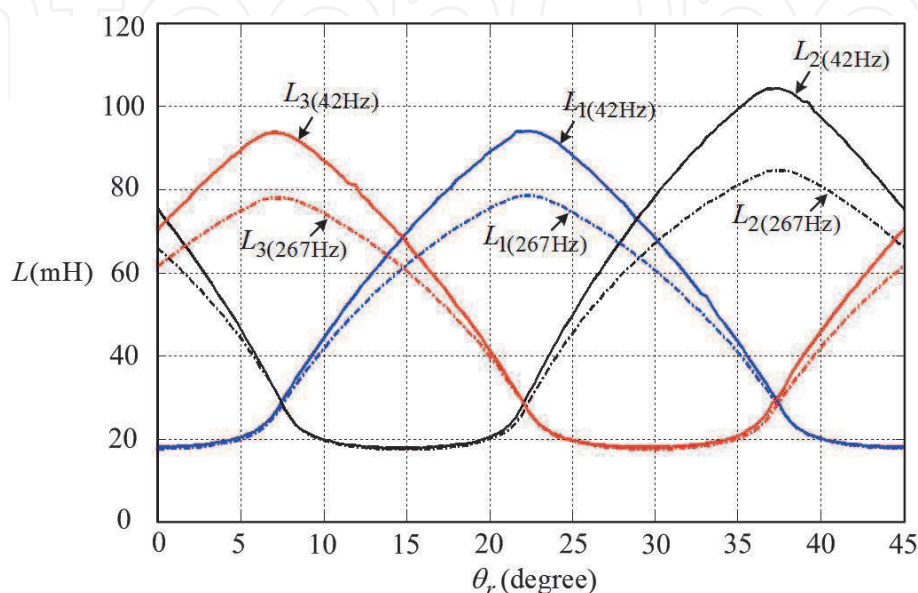

Figure 7.
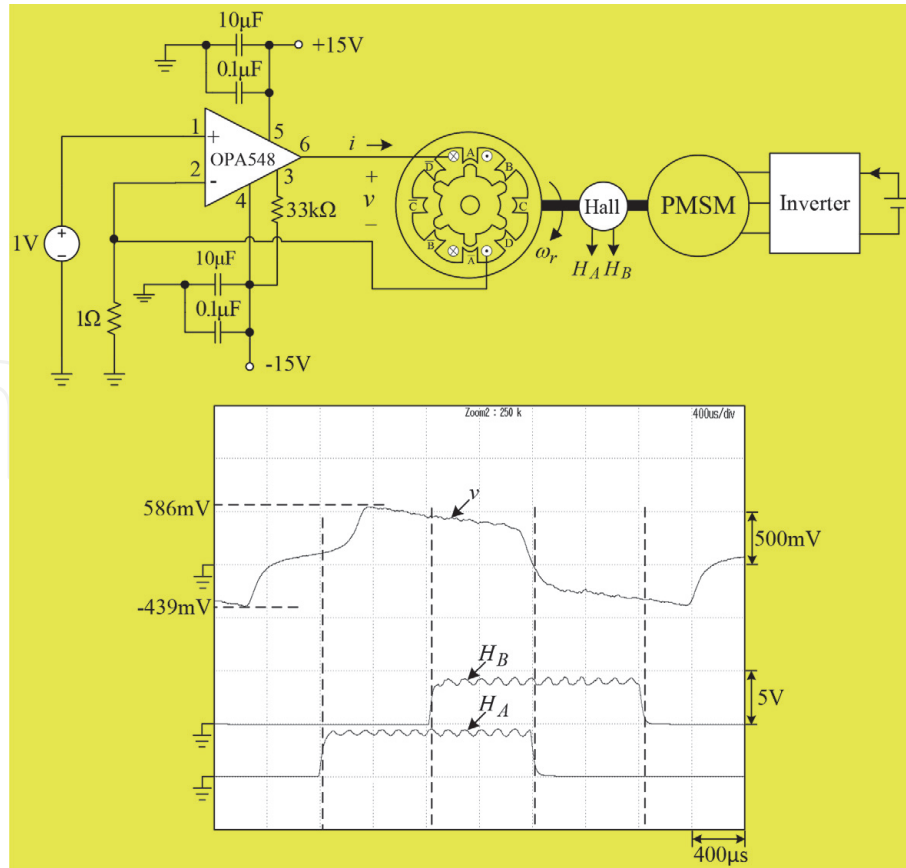*Measured winding inductance profiles of an example three-phase SRM.*

Figure 8.
Measured winding terminal voltage v *and Hall signals of an example SRM by constant current injection at 0.979 A and 3000 rpm.*

Comments: If the driven device for the test SRM is not available, one can turn a rope wound on the motor shaft.

3. Possible front-end converters

3.1 DC/DC front-end converters

The typical system configuration of a battery-powered SRM drive with DC/DC front-end converter is shown in **Figure 9**. The equipped DC/DC converter may possess some merits: (i) the selection of battery voltage is more flexible; (ii) the boostable and well-regulated DC-link voltage can enhance the motor driving performance, especially in high speed and/or heavy load. If the regenerative braking with energy recovery battery charging is desired, the bidirectional DC/DC converter must be employed. **Figure 10(a)** and **(b)** shows two bidirectional front-end DC/DC converters. For the latter, the DC-link voltage can be made smaller or higher than the battery voltage. The motor drive may possess better performance over wider speed range.

3.2 AC/DC front-end converters

For AC power (utility power)-fed SRM drive as indicated in **Figure 9**, one can replace the DC/DC converter with a suited type of boost switch-mode rectifier (SMR). The SMRs can provide boosted and well-regulated DC-link voltage to enhance the motor drive, driving characteristics with good line drawn power
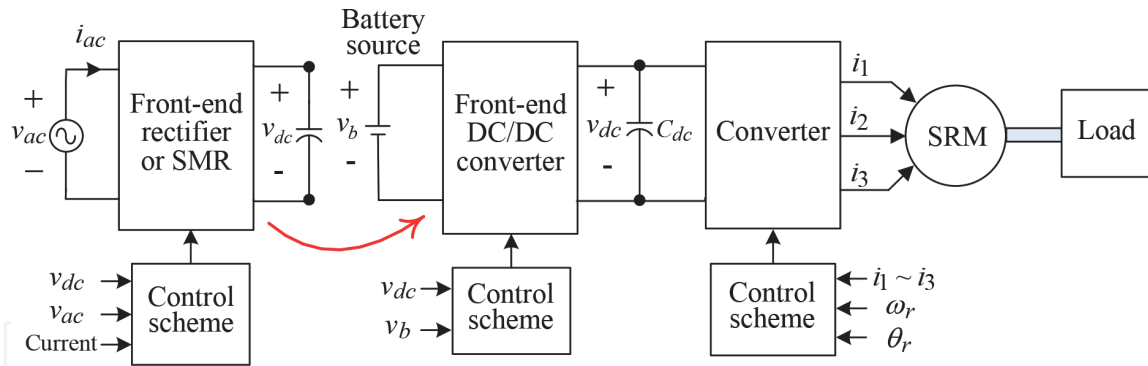
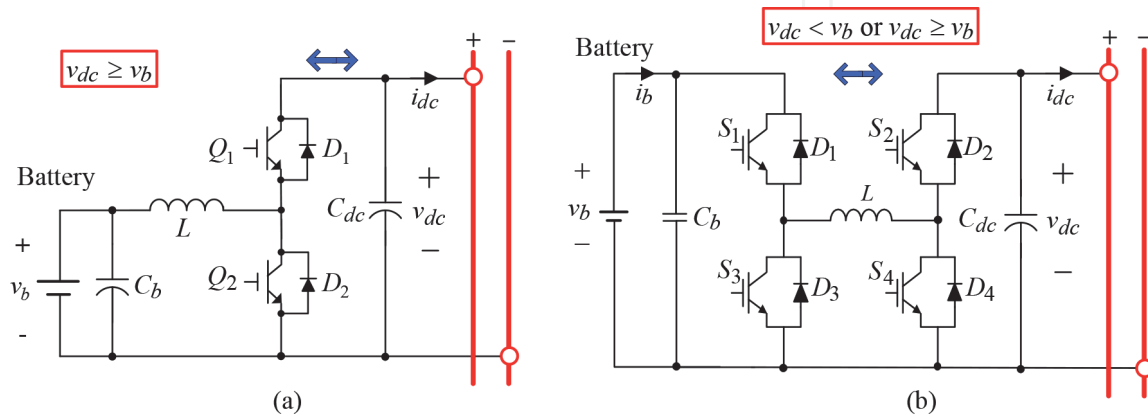**Figure 9.**
A SRM drive with front-end DC/DC converter or SMR.

Figure 10.
Two typical bidirectional interface DC/DC converters: (a) one-leg boost/buck converter; (b) H-bridge four-quadrant converter.
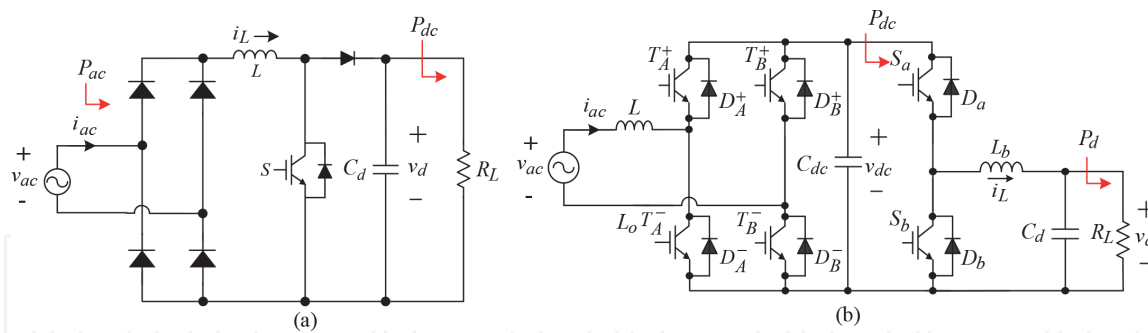

Figure 11.
Two boost type SMRs: (a) unidirectional SMR; (b) bidirectional SMR.

quality. **Figure 11(a)** and **(b)** shows a boost unidirectional SMR and a boost/buck bidirectional SMR. The latter possesses higher flexibility in voltage transfer ratios.

4. Some key issues of SRM and SRG

Some key issues affecting the operating characteristics of an SRM drive and an SRG system are depicted in **Figures 12** and **13**. From Eqs. (3) and (5), one can be aware that commutation angle setting and shifting are the critical factors affecting the SRM and SRG winding current tracking characteristics. Under higher speed and/or heavier load, the DC-link voltage boosting must be adopted. This task can be fulfilled by adding a proper front-end DC/DC converter for battery-powered drive or SMR for utility-powered cases.
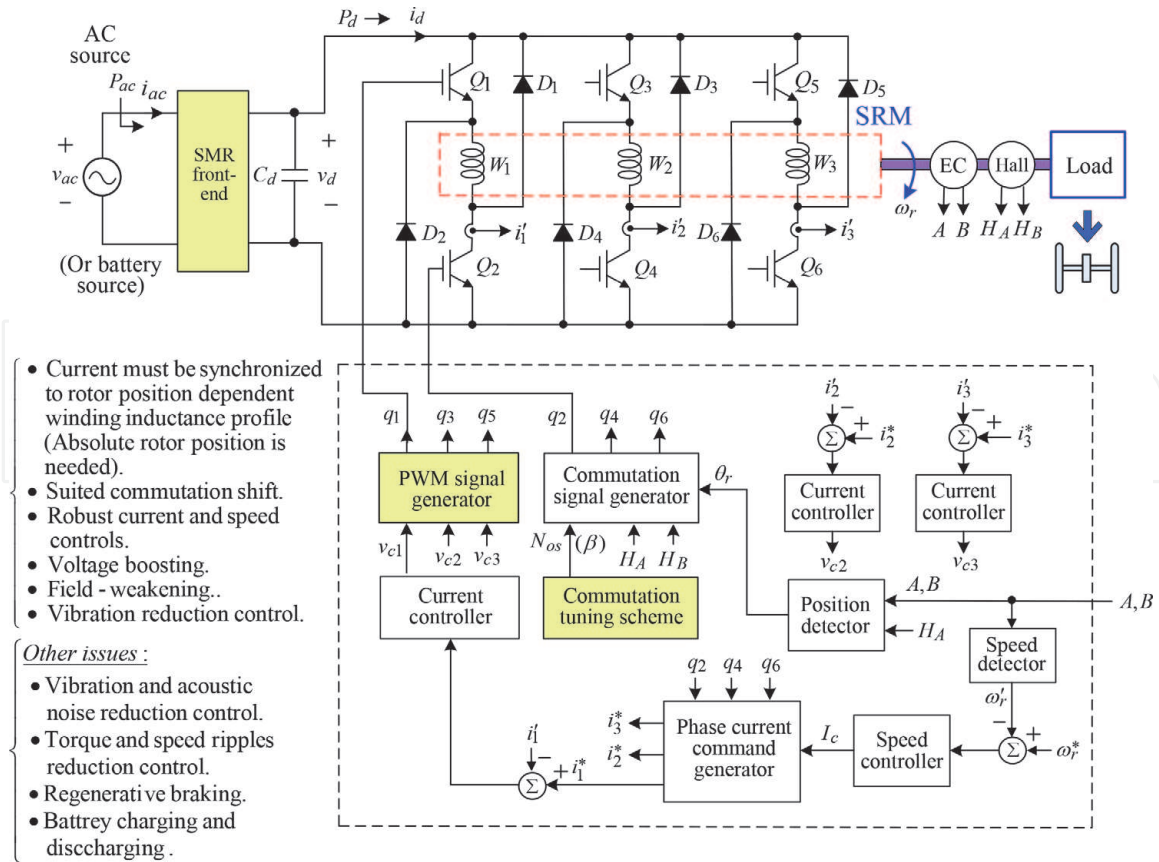
11

Figure 12.
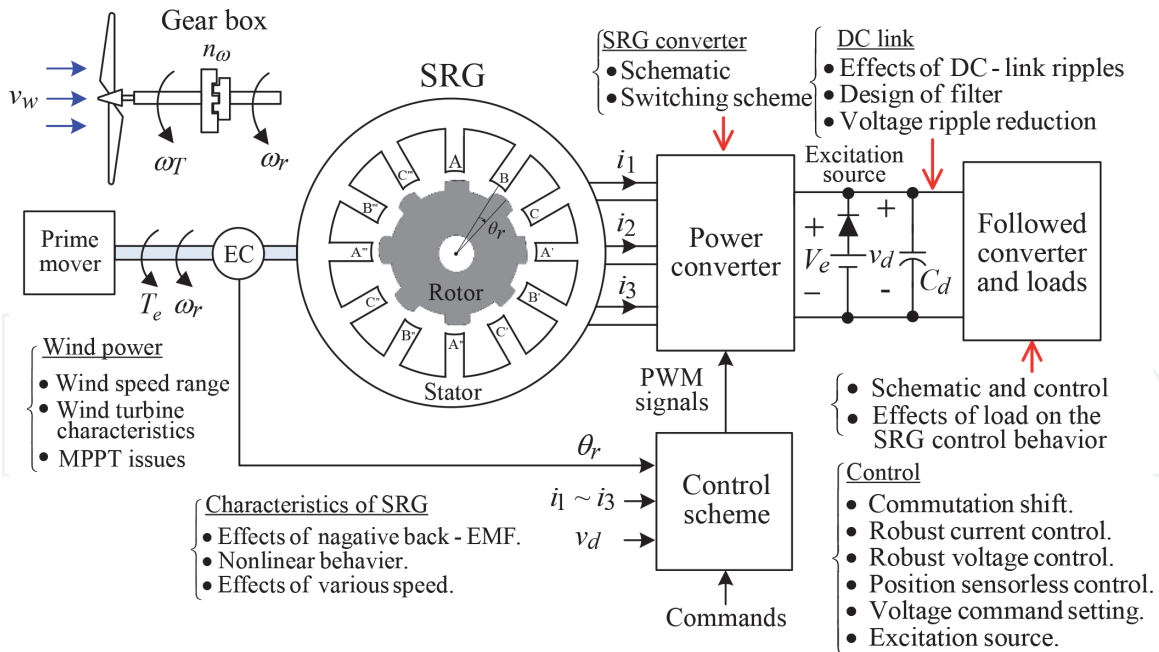*Key issues affecting the performance of an SRM drive.*

Figure 13.
Key issues affecting the performance of an SRG system.

To comprehend the effectiveness of voltage boosting approach, a battery (48 V)-powered SRM drive [26] is equipped with a one-leg boost/buck interface converter as shown in **Figure 10(a)**. **Figure 14(a)** and **(b)**, respectively, shows the measured DC-link voltage V_d, boost switching signal, phase-1 winding current i_1, and its command i_1^* ($\omega_r = 6000$rpm, $R_L = 6.3\ \Omega$, R_L denotes the load resistance of the lad PMSG) under $V_b = 45$ V and $V_d = 45$ V and $V_b = 40$ V and $V_d = 64$ V.
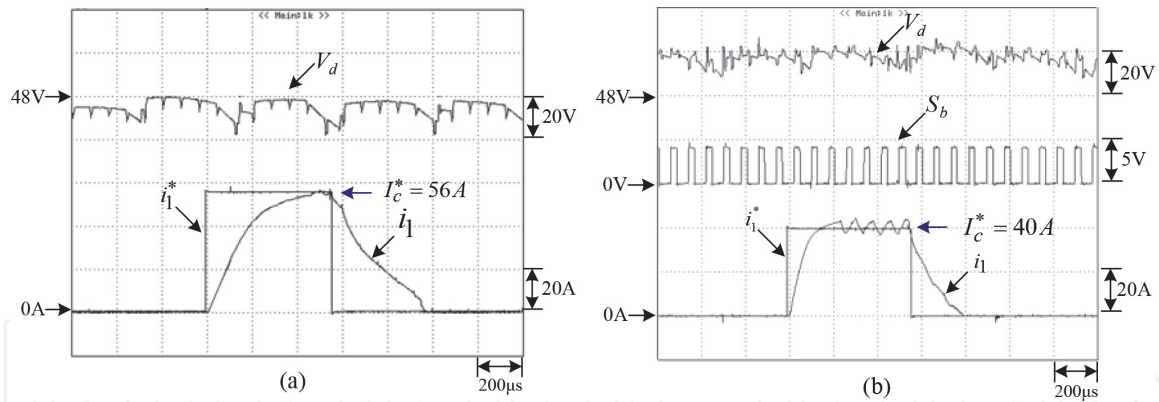
Figure 14.
Measured DC-link voltage V_d, boost switching signal S_b, phase-1 winding current i_1, and its command i_1^* at $\omega_r = 6000rpm$, $R_L = 6.3\ \Omega$: (a) $V_b = 45\ V$ and $V_d = 45\ V$ (fixed) and (b) $V_b = 40\ V$ and $V_d = 64\ V$.

Significant improved winding current response by boosting the DC-link voltage can be observed from the results.

5. Example SRG system: a grid-connected SRG-based microgrid

5.1 System configuration

Figure 15 shows the circuit of the grid-connected SRG-based microgrid with bidirectional 1P3W isolated inverter [27]. The wind SRG is followed by an interleaved DC/DC boost converter to establish the 400 V microgrid common DC bus. The bidirectional isolated 1P3W load inverter with 60 Hz 110 V/220 V AC output voltages is served as a test load. A supercapacitor (SC) placed at the SRG output provides improved voltage regulation caused by fluctuated wind speed. The other energy storage devices and other constituted parts are neglected due to the limit of scope.

The major features of the established SRG system are summarized as (1) SRG, four-phase, 8/6, 48 V, 6000 rpm, 2.32 kW (DENSEI company, Japan);
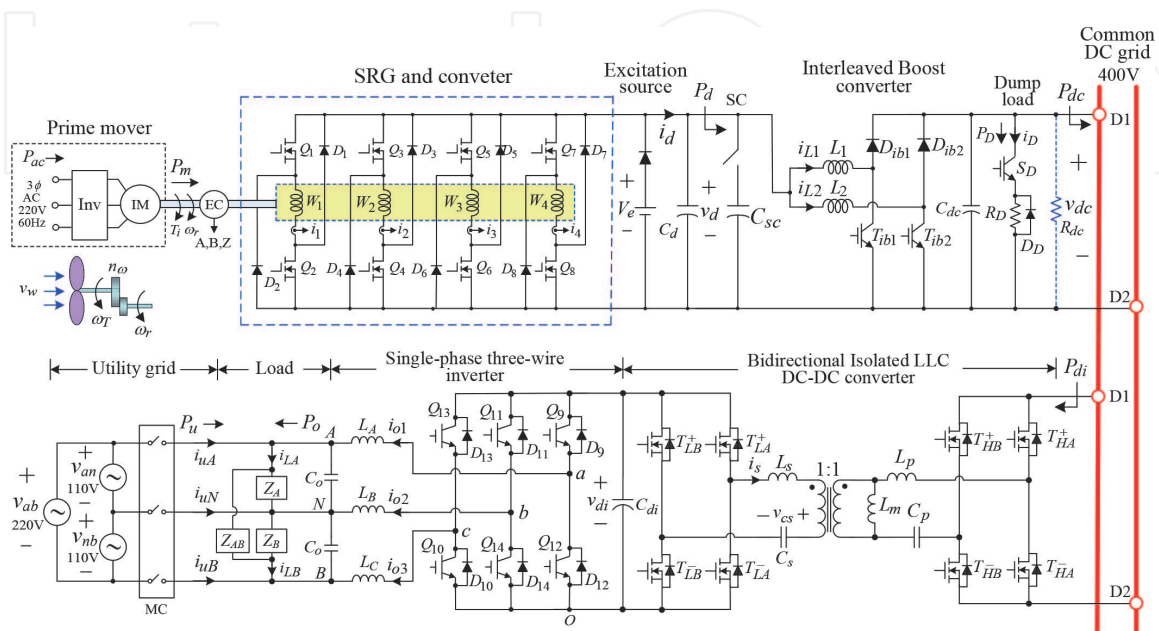

Figure 15.
Schematics of the grid-connected SRG-based microgrid with bidirectional 1P3W isolated inverter.

(2) asymmetric bridge converter, constructed using MOSFET IRLB4030PBF (100 V/180 A (continuous), 730 A (peak)); (3) SC, 48 V/66F; and (4) excitation source, $V_e = 12V$.

The control scheme of wind SRG is shown in **Figure 16**. It consists of an outer-loop voltage controller and an inner-loop HCCPWM scheme. In addition, the dynamic shift controller (DSC) is designed to automatically make the commutation shift according to the average voltage tracking error $\bar{\varepsilon}_v$. On the other hand, since the back-EMF of SRG is proportional to the rotor speed and winding current, the voltage command v_d^* is determined according to rotor speed ω_r and winding current command.

5.2 Some experimental results

5.2.1 SRG-based microgrid

The established wind SRG-powered DC microgrid is evaluated first. **Figure 17 (a)** shows the measured microgrid DC-link voltage v_d, current command i_1^*, and phase-1 winding current i_1 of the SRG under $\omega_r = 6000rpm$, $R_{dc} = 200\Omega$. And **Figure 17(b)** plots the measured output voltage v_{dc}, DC-link current i_d, and inductor currents (i_{L1}, i_{L2}) of the interleaved converter. As a result, the interleaved DC/DC boost interface converter can establish the microgrid common DC bus voltage (400 V) from the SRG output (48 V) successfully.

To evaluate the performance of the microgrid under changed SRG driving speed, at $v_d^* = 48$ V and $v_{dc}^* = 400$ V, the measured ω_r', v_d, and v_{dc} under varying driven speed $\omega_r = 6000 \rightarrow 5000 \rightarrow 6000$ rpm at $R_{dc} = 320$ Ω are shown in **Figure 18**. From the results, one can deduce that the developed DC microgrid owns well-regulated common DC bus voltage under varied SRG driven speed.

5.2.2 Wind SRG-powered DC microgrid with bidirectional 1P3W inverter

5.2.2.1 Microgrid-to-home (M2H) mode

The 1P3W inverter is operated under autonomous M2H mode, and SRG is driven at 6000 rpm. The measured DC-link voltage v_d and the phase-1 winding
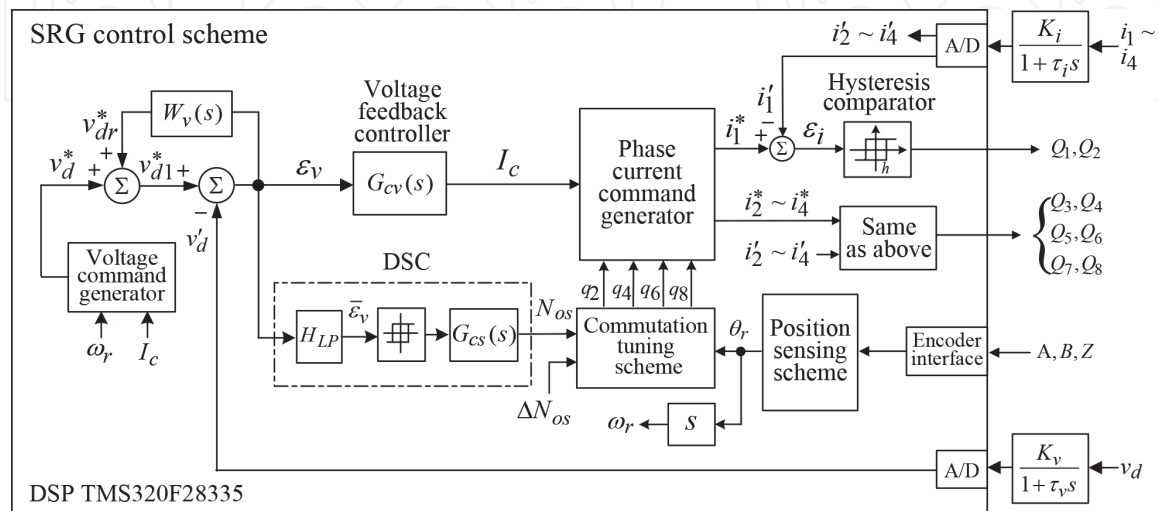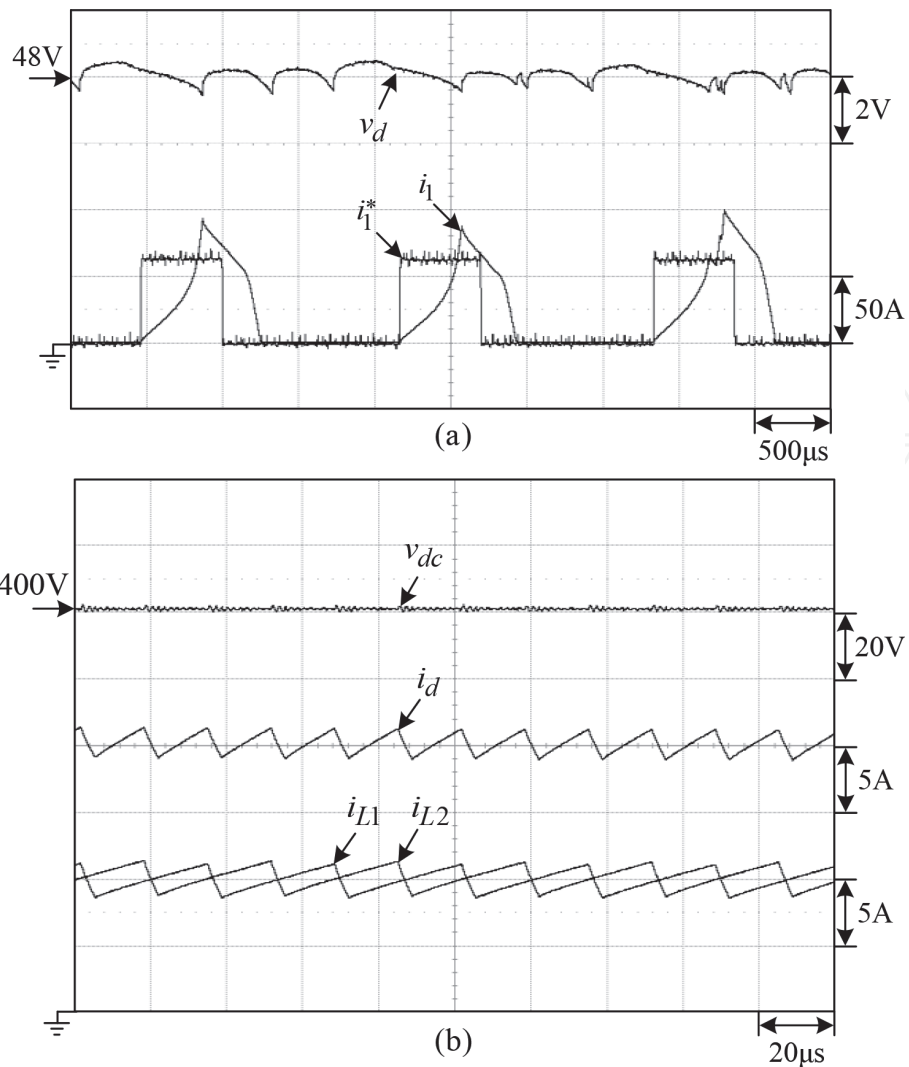

Figure 16.
Control scheme of the wind SRG.

Figure 17.
Measured results of the developed SRG-based DC microgrid at $\omega_r = 6000rpm$, $R_{dc} = 200\ \Omega$: (a) v_d, i_1^*, and i_1 of the SRG stage; (b) v_{dc}, i_d, i_{L1}, and i_{L2} of the interleaved boost interface converter.
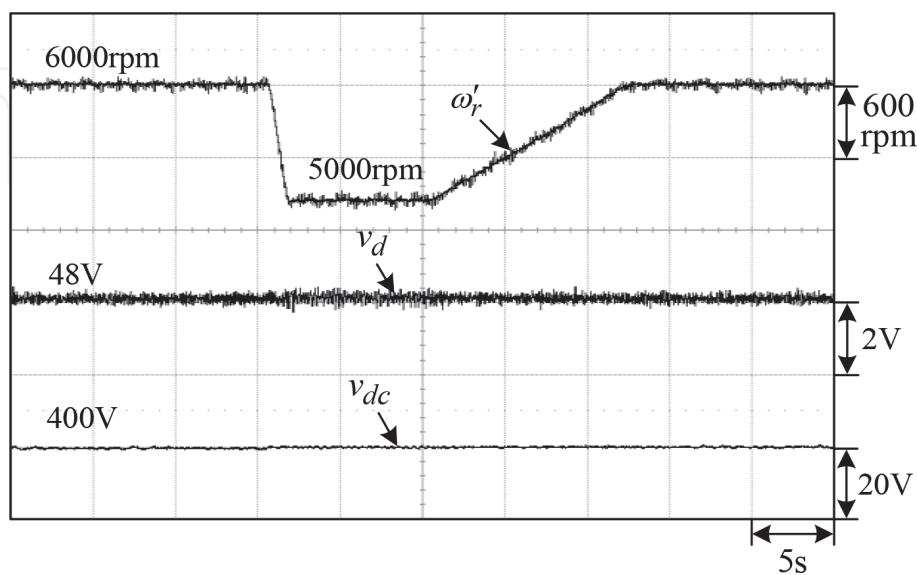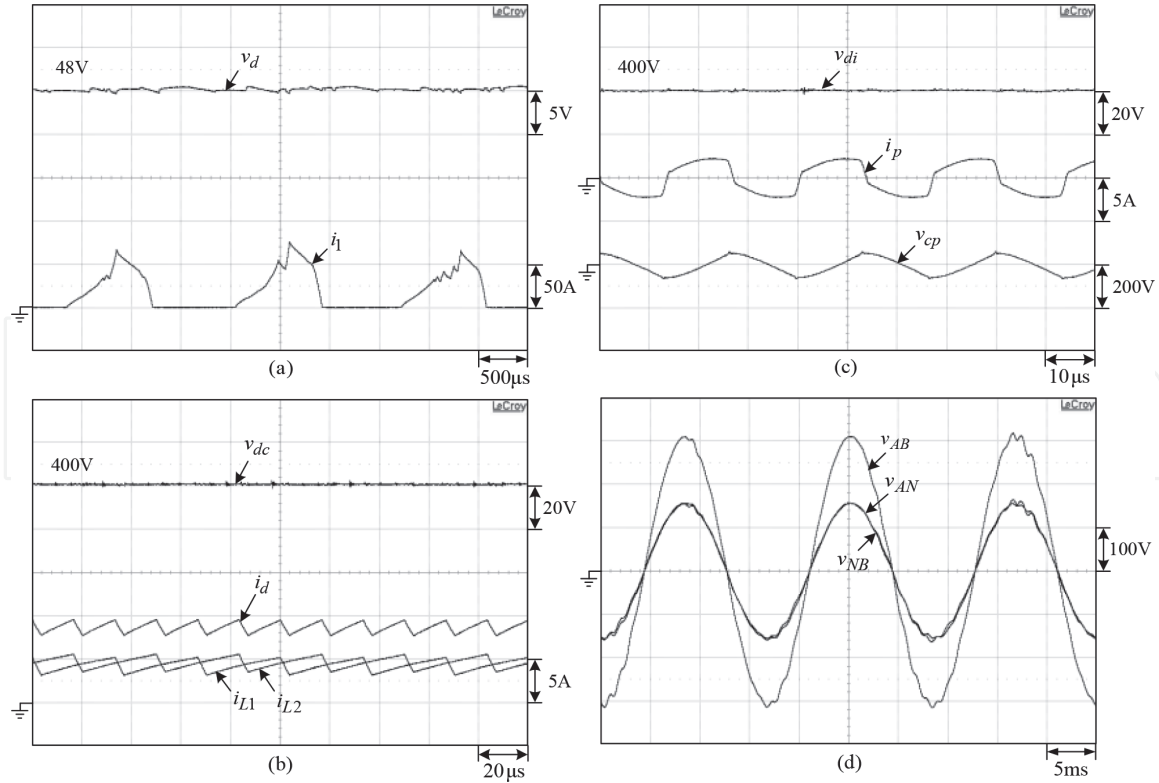

Figure 18.
Measured ω_r', v_d, and v_{dc} of the established SRG-based DC microgrid under varying driven speed $\omega_r = 6000 \rightarrow 5000 \rightarrow 6000\ rpm$ at $R_{dc} = 320\ \Omega$.

15

Figure 19.
Measured results of the established DC microgrid with 1P3W load inverter at $\omega_r = 6000$ rpmand the loads $Z_A = 132.25$ Ω, $Z_B = 132.25$ Ω, and $Z_{AB} = 484$ Ω: (a) (v_d, i_1); (b) $(v_{dc}, i_d, i_{L1}, i_{L2})$; (c) (v_{di}, i_p, v_{cp}); (d) (v_{AB}, v_{AN}, v_{NB}).

current i_1 using PR controller are shown in **Figure 19(a)**. And **Figure 19(b)** shows the DC-link current i_d, the inductor currents (i_{L1}, i_{L2}), and the common DC-bus voltage v_{dc} of the interleaved boost converter. Well-regulated common DC-bus voltage v_{dc}(400 V) is established by the designed interleaved boost converter.

Figure 19(c) shows the measured secondary-side voltage v_{di}, the primary-side resonant capacitor voltage v_{cp}, and the primary-side resonant current i_p of the bidirectional LLC resonant converter. And the measured steady-state waveforms v_{AB}, v_{AN}, and v_{NB} at $Z_A = 132.25$ Ω, $Z_B = 132.25$ Ω , and $Z_{AB} = 484$ Ω are shown in **Figure 19(d)**. The results show that normal M2H operation is achieved.

5.2.2.2 Microgrid-to-grid (M2G) mode

In M2G mode, the SRG is driven at 6000 rpm and the isolated 1P3W inverter is employed. The discharging power command is set as $P_u^* = -800$W, **Figure 20 (a)–(d)** shows the measured steady-state waveforms of (v_d, i_1), $(v_{dc}, i_d, i_{L1}, i_{L2})$, (v_{di}, i_p, v_{cp}), and (v_{AB}, i_{o1}, i_{uA}) of the SRG stage, the interleaved boost converter, the bilateral LLC resonant converter, and the 1P3W inverter under the loads $(Z_A = Z_B = Z_{AB} = \infty)$. According to the experimental results, the M2G operation is achieved with low distortion.

5.2.2.3 Grid-to-microgrid (G2M) mode

The DC bus voltage $v_{dc} = 400$V is established by the bidirectional 1P3W isolated inverter from the mains. And a test load resistor R_{dc} is placed across the DC-bus. The measured (v_{dc}, i_s, v_{cs}) and (v_{di}, v_{ab}, i_{o1}) at $R_{dc} = 200\Omega$ are shown
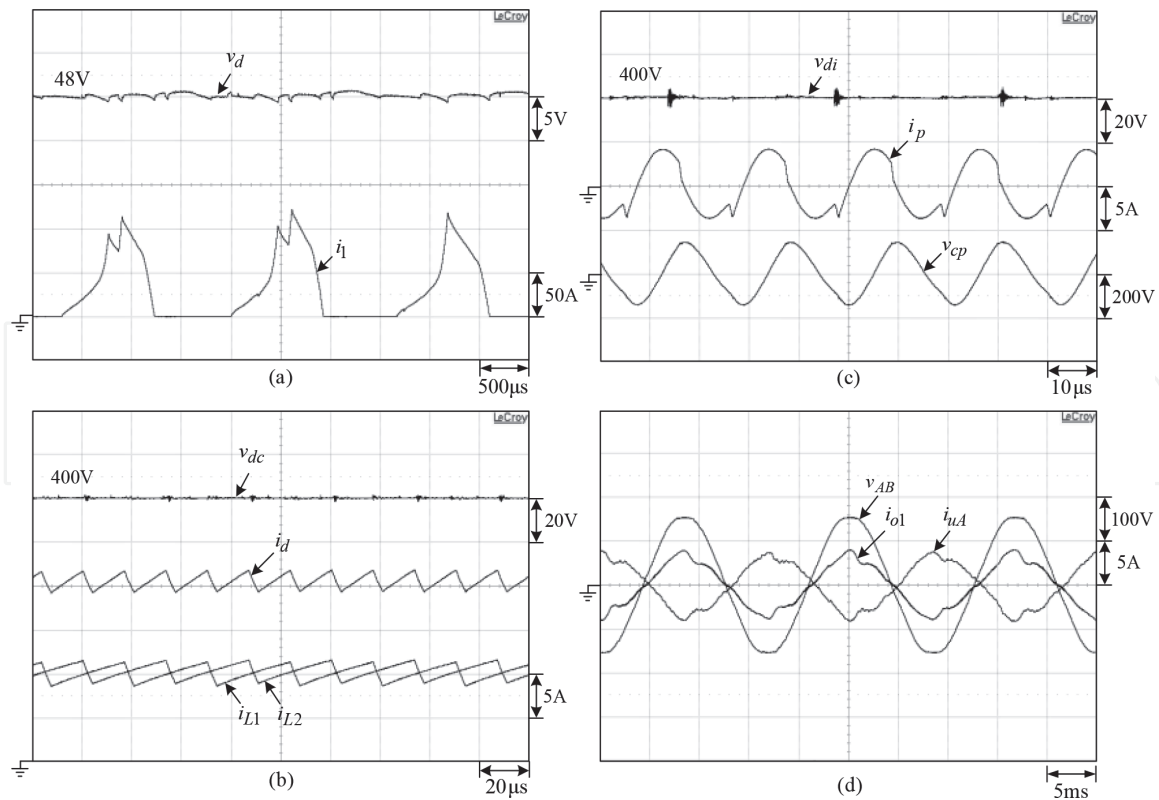
Figure 20.
Measured results of the established DC microgrid with 1P3W load inverter in M2G mode at the power command $(P_u^* = -800\,W)$ *under the loads* $(Z_A = Z_B = Z_{AB} = \infty)$: *(a)* (v_d, i_1); *(b)* $(v_{dc}, i_d, i_{L1}, i_{L2})$; *(c)* (v_{di}, i_p, v_{cp}); *(d)* (v_{AB}, i_{o1}, i_{uA}).
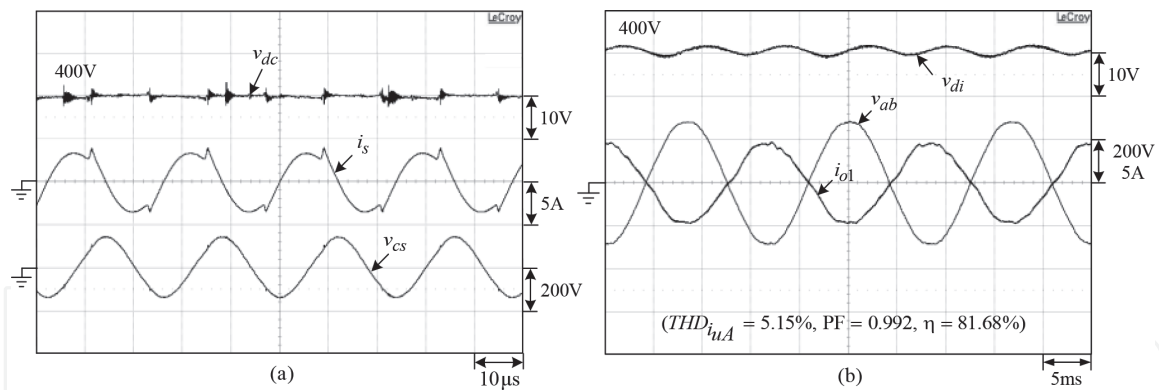

Figure 21.
Measured results of the HF isolated single-phase three-wire load inverter in G2M charging mode with $R_{dc} = 200\ \Omega$: *(a)* (v_{dc}, i_s, v_{cs}); *(b)* (v_{di}, v_{ab}, i_{o1}).

in **Figure 21(a)** and **(b)**. The normal G2M operation can also be observed from the results.

6. Example SRM drive: a battery/SC-powered EV SRM drive

6.1 System configuration

The power circuit of the established EV SRM drive is shown in **Figure 22(a)** [28]. It consists of a battery bank and a SC bank with their bidirectional DC/DC converters, a SRM drive, a test load, and a dynamic brake leg. **Figure 22(b)** shows
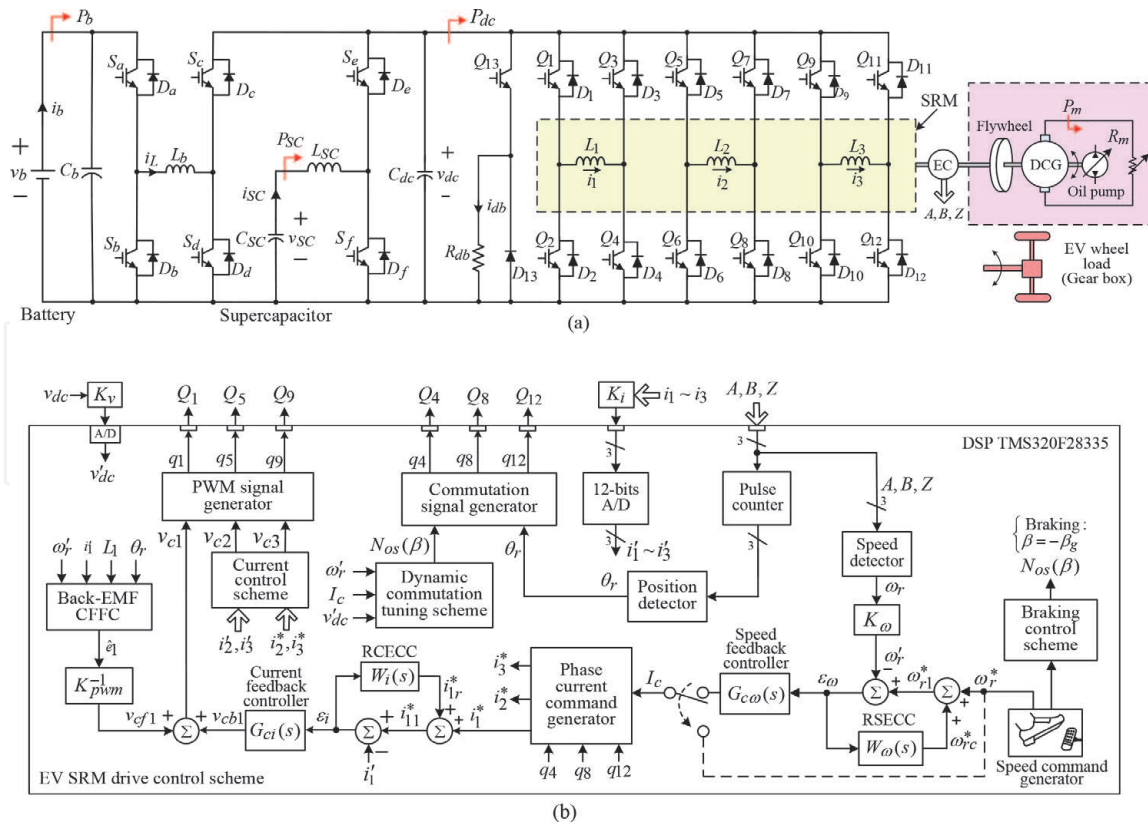
Figure 22.
The EV SRM drive: (a) schematic; (b) SRM drive control scheme.
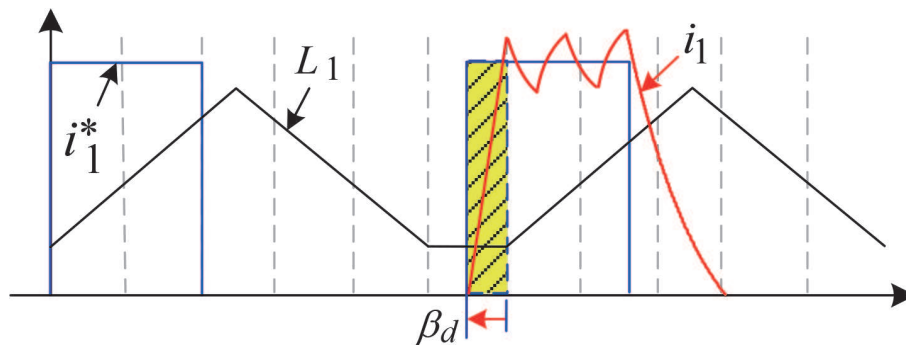

Figure 23.
The proposed dynamic commutation tuning mechanism.

the control scheme of the SRM drive, whereas the control schemes of battery, SC, and dynamic brake are neglected here.

The major features of the developed EV SRM drive are (1) SRM (three-phase, 12/8, 550 V, 1500 rpm, 2.2 kW) and (2) asymmetric bridge converter (it is constructed using two three-phase IGBT modules CM100RL-12NF (Mitsubishi Company)). The switches (Q_1, Q_5, Q_9) are in charge of PWM switching control, and (Q_4, Q_8, Q_{12}) are commutation switches.

The proposed control scheme of the developed SRM drive shown in **Figure 22(b)** consists of the outer speed-loop, the inner current-loop, and a dynamic commutation tuning (DCT) scheme. In the proposed control scheme, the basic feedback controller is augmented with an observed back-EMF current feed-forward controller (CFFC) and a robust current tracking error cancelation controller (RCECC) with the robust weighting factor $W_i(s) = W_i/(1 + \tau_i s)$, $W_i = 0.4$, $\tau_i = 2.6525 \times 10^{-4} s$. The DCT scheme is proposed here to conduct the commutation shift automatically. As shown in **Figure 23**, in order to let the winding current be the commanded value within the

advanced shift angle in the minimum and constant inductance region, from the voltage equation listed in Eq. (3), one can obtain:

$$v_{dc} = Ri + e(i, \omega_r, \theta_r) + L(i, \theta_r)\frac{di}{dt} \cong L_{\min}\frac{I_c}{\Delta T_\beta} \qquad (15)$$

where ΔT_β denotes the advanced shifting time interval within which the winding current being linearly risen to I_c, where $R \cong 0$, $\partial L(i, \theta_r)/\theta_r = 0$, $e(i, \omega_r, \theta_r) = 0$ and $L(i, \theta_r) = L_{\min}$ are assumed. Thus, the required dynamic commutation advanced shift angle β_d can be derived from Eq. (15):

$$\beta_d = \Delta T_\beta \omega_r = \frac{L_{\min}}{v_{dc}} I_c \omega_r \qquad (16)$$

6.2 Some experimental results

6.2.1 Winding current responses

Figure 24(a)–(c) shows the measured (i_1^*, i_1) at ($V_{dc} = 550$ V, $R_m = 320$ Ω, $\omega_r = 1000$ rpm) by the PI control augmented with the back-EMF CFFC and the RCECC, respectively. Obviously, the effectiveness of the proposed current control methods can be observed from the results. **Figure 25(a)** and **(b)** shows the
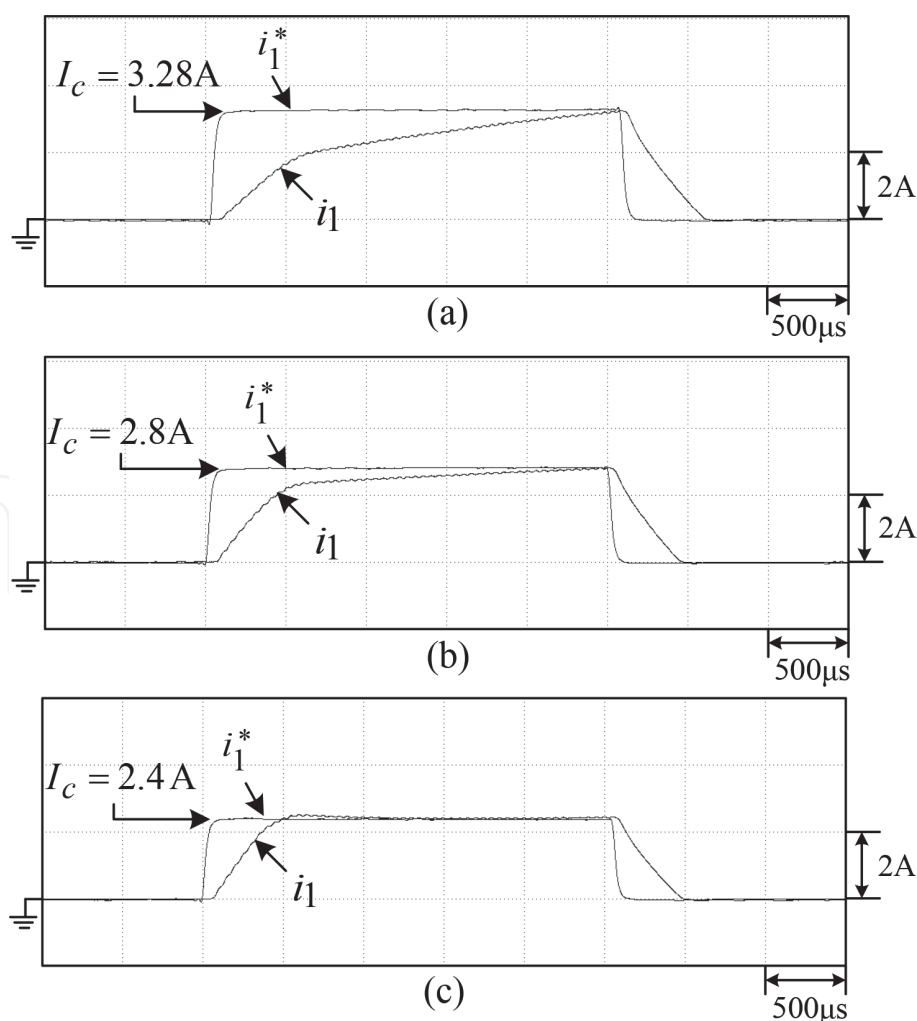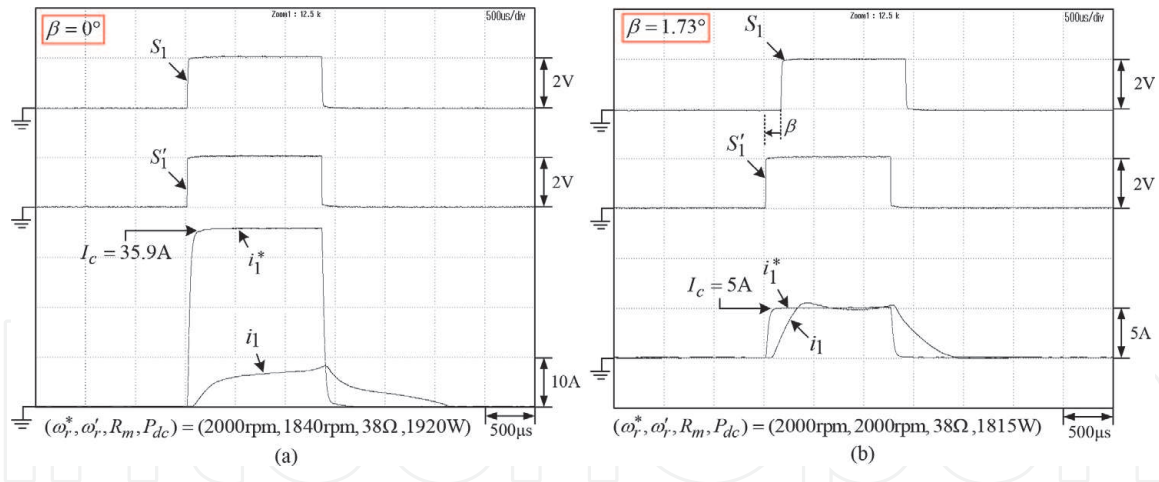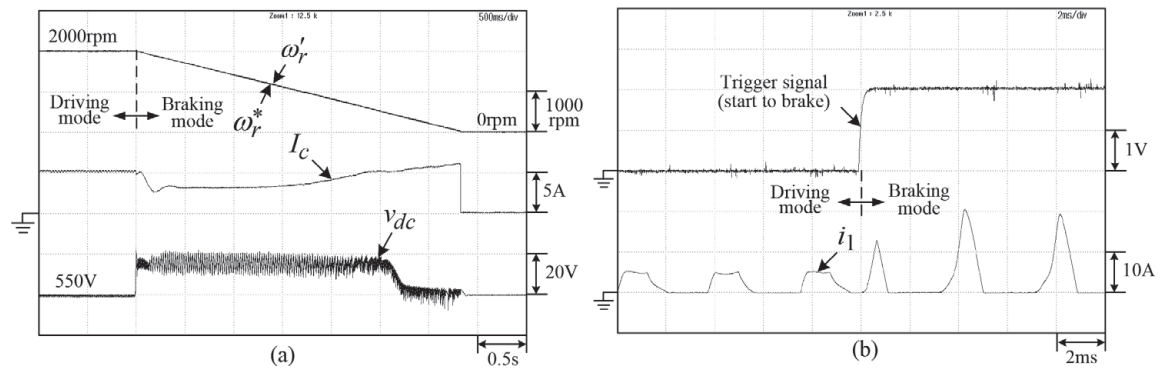

Figure 24.
Measured phase-1 winding at $R_m = 320$ Ω, $\omega_r = 1000$ rpm) :(a) PI only; (b) PI and back-EMF CFFC; (c) PI, back-EMF CFFC, and RCECC.

Figure 25.
Measured $\left(i_1^*, i_1\right)$ of phase-1 winding at $(V_{dc} = 550\ V, R_m = 37.33\ \Omega, \omega_r = 2000\ rpm)$ by all controls without and with dynamic commutation tuning: (a) without DCT, $\beta = 0°$; (b) with DCT, $\beta = 1.73°$.

Figure 26.
Measured results during braking by letting the speed command be changed from $\omega_r^* = 2000\ rpm$ to $0\ rpm$ with $600\ rpm/s$ falling rate: (a) speed command ω_r^*, speed ω_r', winding current command I_c, and DC-link voltage v_{dc}; (b) trigger signal and phase-1 winding current i_1.

measured $\left(i_1^*, i_1\right)$ by all controls at $(V_{dc} = 550\ V, R_m = 37.33\ \Omega,\ \omega_r = 2000\ rpm)$ without and with DCT. One can observe applying DCT can let the winding current tracking control be improved.

6.2.2 Regenerative braking

By exciting the winding under the negative winding inductance slope region, the SRM will be operated as an SRG. The SRM is initially driven to 2000 rpm under V_{dc} = 550 V, ω_r = 2000 rpm, and R_m = 61.3 Ω. Then the speed command is set from $\omega_r^* = 2000\ rpm$ to 0 rpm with 600 rpm/s decelerating rate. The measured speed command ω_r^*, speed ω_r', winding current command I_c, and DC-link voltage v_{dc} are shown in **Figure 26(a)**. **Figure 26(b)** confirms the successful SRG operation during regenerative braking from the winding current waveform.

6.2.3 Performance evaluation of the established EV SRM drive

6.2.3.1 Battery only

First, let the SRM drive be powered by battery only; the measured $\left(\omega_r', \omega_r^*, v_b, i_b, v_{dc}\right)$ at $(V_b = 156\ V,\ V_{dc} = 550\ V, R_m = 455\ \Omega)$ due to the speed

command setting of $\omega_r^* = 0$ rpm $\rightarrow$ 2000 rpm $\rightarrow$ 1500 rpm $\rightarrow$ 2000 rpm $\rightarrow$ 1000 rpm $\rightarrow$ 2000 rpm $\rightarrow$ 0 rpm with rising rate and falling rate both 300 rpm/s are shown in **Figure 27**. Normal speed tracking and battery discharging/charging characteristics are seen from the results.
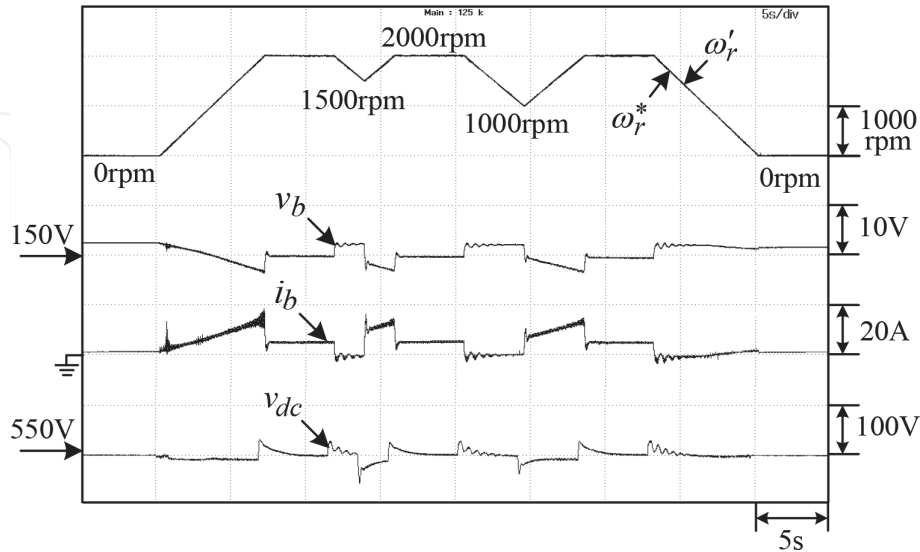

Figure 27.
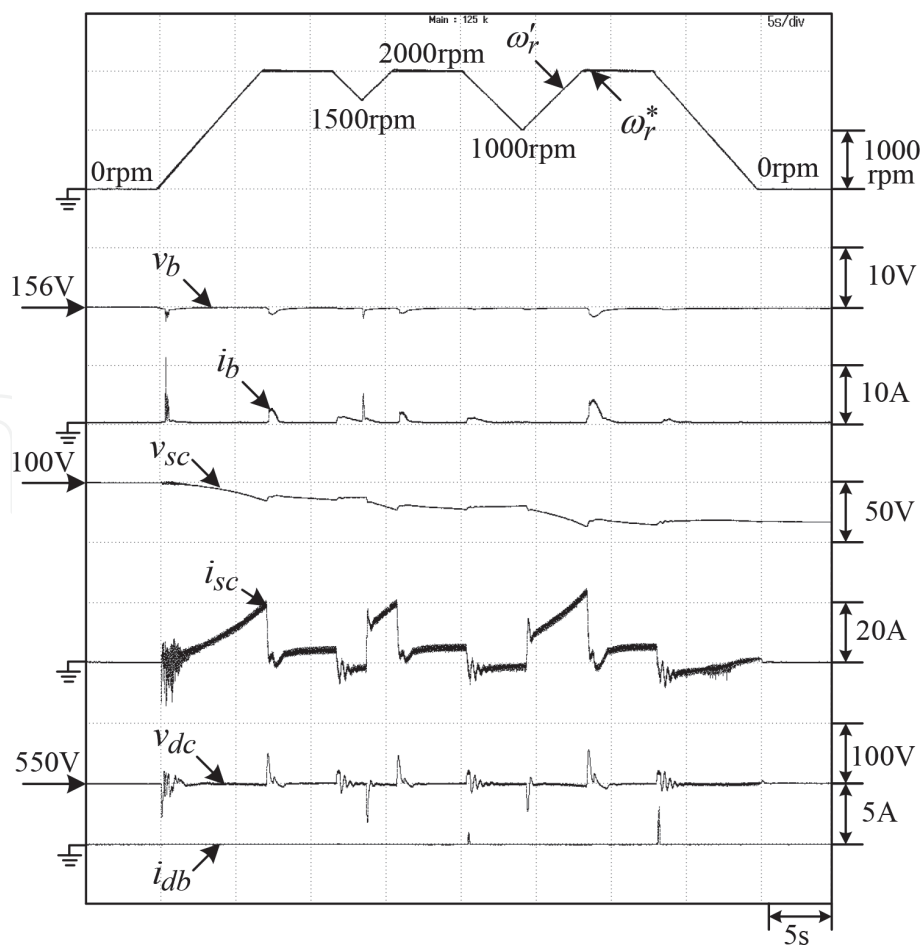*The EV SRM drive powered by battery only at $V_b = 156V$, $V_{dc} = 550$ V, $R_m = 455\Omega$).*

Figure 28.
The EV SRM drive powered by battery and SC at ($V_b = 156$ V, $V_{SC} = 100$ V, $V_{dc} = 550$ V, $R_m = 455$ Ω).

6.2.3.2 Battery and supercapacitor

The measured $(\omega'_r, \omega^*_r, v_b, i_b, v_{sc}, i_{sc}, v_{dc}, i_{db})$ of the battery/SC hybrid energy-powered EV SRM drive at $(V_b = 156V, V_{SC} = 100V, V_{dc} = 550V, R_m = 455\ \Omega)$ due to the speed command setting of ω^*_r = 0 rpm → 2000 rpm → 1500 rpm → 2000 rpm → 1000 rpm → 2000 rpm → 0 rpm with rising rate and falling rate both 300 rpm/s are shown in **Figure 28**. Compared to **Figure 27**, much smaller battery discharging currents are yielded thanks to the assistance of SC.

6.2.3.3 (c) Varied DC-link voltage

The DC-link voltage setting approaches used for comparison are shown in **Figure 29**, which are listed below:

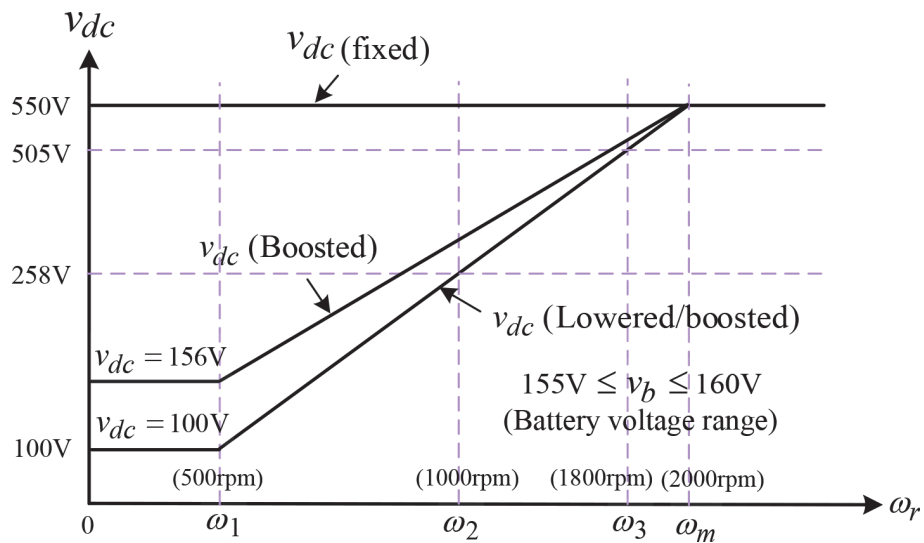1. Fixed DC-link voltage: V_{dc} = 550 V $(0 \leq \omega_r \leq 2000\ rpm)$

Figure 29.
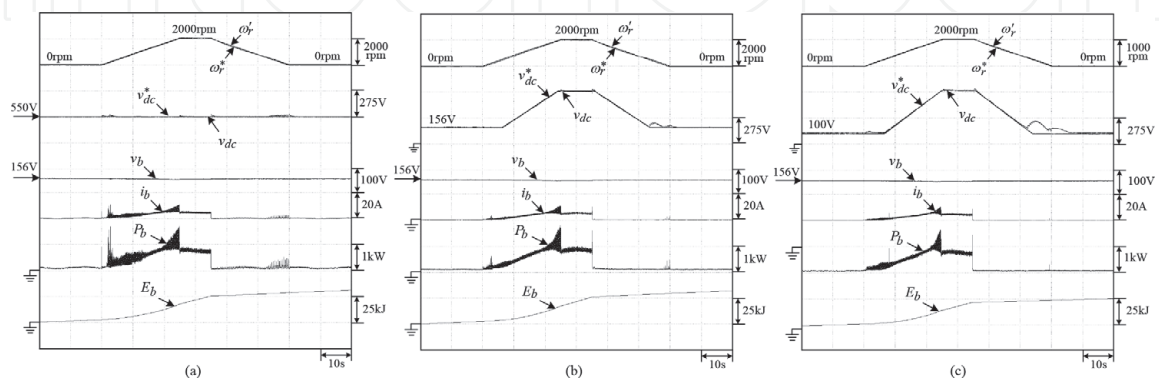*Voltage profiles of DC-link versus motor speed.*

Figure 30.
Measured results of the SRM drive powered by the battery due to ramp speed command change with changing rate of 80 rpm/s at $R_m = 322\Omega$ and $\omega_r = 0$ rpm → 2000 rpm → 0 rpm: (a) fixed voltage ($V_{dc} = 550$ V); (b) boosted voltage ($V_b \leq V_{dc}$); (c) with lowered/boosted voltage ($V_b \geq V_{dc}$ or $V_b \leq V_{dc}$).
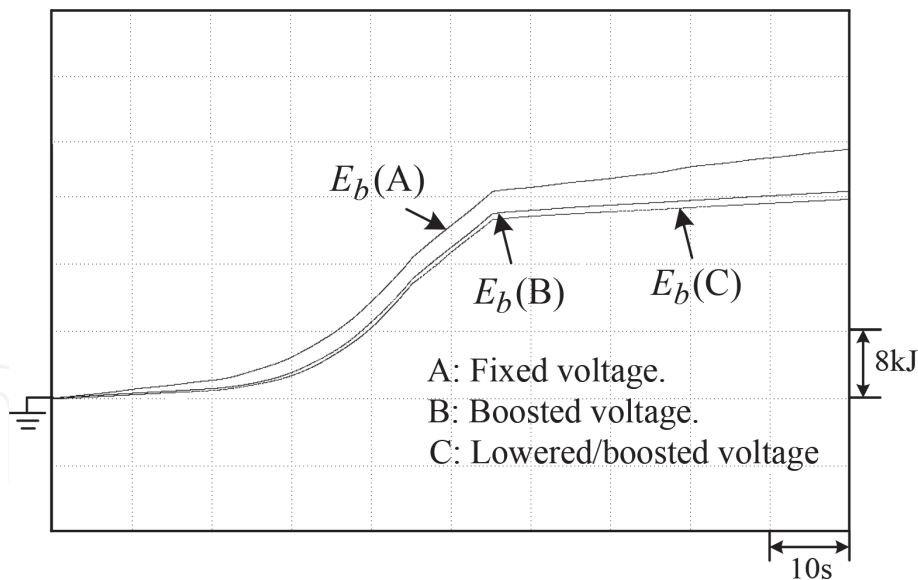
Figure 31.
Measured energies of battery of the developed standard SRM drive powered by battery with three DC-link voltage setting approaches due to ramp speed command change with changing rate of 80 rpm/s at $R_m = 322$ Ω and $\omega_r = 0$ rpm → 2000 rpm → 0 rpm.

2. Varied DC-link voltage:

     i. Boosted DC-link voltage: $V_b = 156$ V, $V_{dc} = 156$ V $(0 \leq \omega_r \leq 500$ rpm); $156 < V_{dc} \leq 550$ V $(500 < \omega_r \leq 2000$ rpm).

     ii. Lowered and boosted DC-link voltage: $V_b = 156$ V, $V_{dc} = 100$ V $(0 \leq \omega_r \leq 500$ rpm); $100 < V_{dc} \leq 550$ V $(500 < \omega_r \leq 2000$ rpm).

Figure 30(a)–(c) shows the measured results of the developed EV SRM drive under three DC-link voltage setting approaches. And the energies of battery are compared in **Figure 31**. From **Figure 31**, the effectiveness in energy saving by applying the lowered/boosted DC-link voltage over the boosted and the fixed ones can be observed.

7. Conclusions

Compared to other machines, SRM is more difficult to control for yielding satisfactory operating characteristics. This chapter has presented some basic and key issues for SRM operated as motor and generator. These include structural features, governing equations and dynamic model, SRM converter, some front-end DC/DC converters and SMRs, some key motor parameter estimation and experimental performance evaluation of an SRM drive, commutation scheme, dynamic controls, reversible and regenerative braking operation controls, operation control and tuning issues of SRM and SRG, etc. Finally, two example SRM plants are presented to demonstrate the affairs being described, including a wind SRM based microgrid and an EV SRM drive.

Author details

Chang-Ming Liaw*, Min-Ze Lu, Ping-Hong Jhou and Kuan-Yu Chou
Department of Electrical Engineering, National Tsing Hua University, Hsinchu,
Taiwan, ROC

*Address all correspondence to: cmliaw@ee.nthu.edu.tw

IntechOpen

References

[1] Sen PC. Principles of Electric Machines and Power Electronics. 3rd ed. New Jersey: John Wiley & Sons, Inc.; 2014

[2] Miller TJE. Switched Reluctance Motors and their Control. Oxford: Clarendon Press; 1993

[3] Y Z, Shang F, Brown IP, Krishnamurthy M. Comparative study of interior permanent magnet, induction, and switched reluctance motor drives for EV and HEV applications. IEEE Transactions on Transportation Electrification. 2015;**1**(3):245-254

[4] Bartolo JB, Degano M, Espina J, Gerada C. Design and initial testing of a high-speed 45-kW switched reluctance drive for aerospace application. IEEE Transactions on Industrial Electronics. 2017;**64**(2):988-997

[5] Namazi MM, Nejad SMS, Tabesh A, Rashidi A, Liserre M. Passivity-based control of switched reluctance-based wind system supplying constant power load. IEEE Transactions on Industrial Electronics. 2018;**65**(12):9550-9560

[6] Santos Neto PJD, Santos Barros TAD, Paula MVD, Souza RRD, Filho ER. Design of computational experiment for performance optimization of a switched reluctance generator in wind system. IEEE Transactions on Energy Conversion. 2018;**33**(1):406-419

[7] Miller TJE. Optimal design of switched reluctance motors. IEEE Transactions on Industrial Electronics. 2002;**49**(1):15-27

[8] Schulz SE, Rahman KM. High-performance digital PI current regulator for EV switched reluctance motor drives. IEEE Transactions on Industry Applications. 2003;**39**(4):1118-1126

[9] Lin Z, Reay D, Williams B, He X. High-performance current control for switched reluctance motors based on on-line estimated parameters. IET Electric Power Applications. 2010;**4**(1):67-74

[10] Hwu KI, Liaw CM. Quantitative speed control for SRM drive using fuzzy adapted inverse model. IEEE Transactions on Aerospace and Electronic Systems. 2002;**38**(3):955-968

[11] Hwu KI, Liaw CM. Intelligent tuning of commutation for maximum torque capability of a switched reluctance motor. IEEE Transactions on Energy Conversion. 2003;**18**(1):113-120

[12] Hu KW, Chen YY, Liaw CM. A reversible position sensorless controlled switched-reluctance motor drive with adaptive and intuitive commutation tuning. IEEE Transactions on Power Electronics. 2015;**30**(7):3781-3793

[13] Huang HN, Hu KW, Wu YW, Jong TL, Liaw CM. A current control scheme with back-EMF cancellation and tracking error adapted commutation shift for switched-reluctance motor drive. IEEE Transactions on Industrial Electronics. 2016;**63**(12):7381-7392

[14] Chan S, Bolton HR. Performance enhancement of single-phase switched reluctance motor by DC link voltage boosting. IEE Proceedings B—Electric Power Applications. 1993;**140**(5):316-322

[15] Hwu KI, Liaw CM. DC-link voltage boosting and switching control for switched reluctance motor drives. IEE Proceedings—Electric Power Applications. 2000;**147**(5):337-344

[16] Chang HC, Liaw CM. Development of a compact switched-reluctance motor drive for EV propulsion with voltage

boosting and PFC charging capabilities. IEEE Transactions on Vehicular Technology. 2009;**58**(7):3198-3215

[17] Chai JY, Chang YC, Liaw CM. On the switched-reluctance motor drive with three-phase single-switch switch-mode rectifier front-end. IEEE Transactions on Power Electronics. 2010;**25**(5):1135-1148

[18] Torrey DA. Switched reluctance generators and their control. IEEE Transactions on Industrial Electronics. 2002;**49**(1):3-14

[19] Chang YC, Liaw CM. On the design of power circuit and control scheme for switched reluctance generator. IEEE Transactions on Power Electronics. 2008;**23**(1):445-454

[20] Santos Barros TAD, Santos Neto PJD, Filho PSN, Moreira AB, Filho ER. An approach for switched reluctance generator in a wind generation system with a wide range of operation speed. IEEE Transactions on Power Electronics. 2017;**32**(11): 8277-8292

[21] Rahmanian E, Akbari H, Sheisi GH. Maximum power point tracking in grid connected wind plant by using intelligent controller and switched reluctance generator. IEEE Transactions on Sustainable Energy. 2017;**8**(3): 1313-1320

[22] Vukosavic S, Stefanovic VR. SRM inverter topologies: A comparative evaluation. IEEE Transactions on Industry Applications. 1991;**27**(6): 1034-1049

[23] Barnes M, Pollock C. Power electronic converters for switched reluctance drives. IEEE Transactions on Power Electronics. 1998;**13**(6): 1100-1111

[24] Cabezuelo D, Andreu J, Kortabarria I, Ibarra E, Garate I. SRM converter topologies for EV application: State of the technology. IEEE ISIE. 2017: 861-866

[25] Pereira M, Esteves Araújo R. Analysis and design of a speed controller for switched reluctance motor drive. U. Porto Journal of Engineering. 2019;**5**(1): 46-58

[26] Chang HC. Development of battery powered switched-reluctance motor drives [Ph.D. dissertation]. R.O.C.: Dept. Electric Eng., National Tsing Hua Univ.; 2010

[27] Jhou PH. A wind switched-reluctance generator based grid-connected micro-grid [master thesis]. Hsinchu, ROC: Department of Electrical Engineering, National Tsing Hua University; 2017

[28] Chou KY. A batter/supercapacitor powered EV SRM drive with bidirectional isolated charger [master thesis]. Hsinchu, ROC: Department of Electrical Engineering, National Tsing Hua University; 2017